A&A 673, A85 (2023)
https://doi.org/10.1051/0004-6361/202345936

Astronomy & Astrophysics

Long-term *Swift* and Metsähovi monitoring of SDSS J164100.10+345452.7 reveals multi-wavelength correlated variability

P. Romano[1], A. Lähteenmäki[2,3], S. Vercellone[1], L. Foschini[1], M. Berton[4], C. M. Raiteri[5], V. Braito[1,6,7], S. Ciroi[8], E. Järvelä[9,10], S. Baitieri[11,1], I. Varglund[2,3], M. Tornikoski[2], and S. Suutarinen[2]

[1] INAF, Osservatorio Astronomico di Brera, Via Emilio Bianchi 46, 23807 Merate (LC), Italy
e-mail: patrizia.romano@inaf.it
[2] Aalto University Metsähovi Radio Observatory, Metsähovintie 114, 02540 Kylmälä, Finland
[3] Aalto University Department of Electronics and Nanoengineering, PO Box 15500, 00076 Aalto, Finland
[4] European Southern Observatory (ESO), Alonso de Córdova 3107, Casilla 19, Santiago 19001, Chile
[5] INAF, Osservatorio Astrofisico di Torino, Via Osservatorio 20, 10025 Pino Torinese (TO), Italy
[6] Department of Physics, Institute for Astrophysics and Computational Sciences, The Catholic University of America, Washington, DC 20064, USA
[7] Dipartimento di Fisica, Università di Trento, Via Sommarive 14, Trento 38123, Italy
[8] Dipartimento di Fisica e Astronomia, Università di Padova, 35122 Padova, Italy
[9] European Space Agency, European Space Astronomy Centre, C/ Bajo el Castillo s/n, 28692 Villanueva de la Cañada, Madrid, Spain
[10] Homer L. Dodge Department of Physics and Astronomy, The University of Oklahoma, 440 W. Brooks St., Norman, OK 73019, USA
[11] Università degli Studi di Milano, Bicocca, Piazza delle Scienze 3, 20126 Milano, Italy

Received 18 January 2023 / Accepted 8 March 2023

ABSTRACT

We report on the first multi-wavelength *Swift* monitoring campaign performed on SDSS J164100.10+345452.7, a nearby narrow-line Seyfert 1 galaxy that had formerly been considered to be radio-quiet. It has, however, more recently been detected both in the radio (at 37 GHz) and in the γ-ray, a behaviour that hints at the presence of a relativistic jet. During our 20-month *Swift* campaign, while pursuing the primary goal of assessing the baseline optical/UV and X-ray properties of SDSS J164100.10+345452.7, we observed two radio flaring episodes, namely, one each year. Our strictly simultaneous multi-wavelength data closely match the radio flare and allow us to unambiguously link the jetted radio emission of SDSS J164100.10+345452.7. Indeed, for the X-ray spectra preceding and following the radio flare, a simple absorbed power-law model does not offer an adequate description and, thus, an extra absorption component is required. The average spectrum of SDSS J164100.10+345452.7 can best be described by an absorbed power-law model with a photon index $\Gamma = 1.93 \pm 0.12$, modified by a partially covering neutral absorber with a covering fraction of $f = 0.91^{+0.02}_{-0.03}$. On the contrary, the X-ray spectrum closest to the radio flare does not require any such extra absorber and it is much harder ($\Gamma_{\rm flare} \sim 0.7 \pm 0.4$), thus implying the emergence of an additional, harder spectral component. We interpret this as the jet emission emerging from a gap in the absorber. The fractional variability we derived in the optical/UV and X-ray bands is found to be lower than the typical values reported in the literature because our observations of SDSS J164100.10+345452.7 are dominated by the source being in a low state, as opposed to the literature, where the observations were generally taken as a follow-up of bright flares in other energy bands. Based on the assumption that the origin of the 37 GHz radio flare is the emergence of a jet from an obscuring screen also observed in the X-ray, the derived total jet power is $P^{\rm tot}_{\rm jet} = 3.5 \times 10^{42}$ erg s^{-1}. This result is close to the lowest values measured in the literature.

Key words. galaxies: Seyfert – galaxies: individual: SDSS J164100.10+345452.7 – galaxies: active – X-rays: individuals: SDSS J164100.10+345452.7

1. Introduction

Narrow-line Seyfert 1 galaxies (NLS1s) are active galactic nuclei (AGN) characterised in the optical regime by narrow permitted emission lines (Hβ FWHM < 2000 km s^{-1}, Goodrich 1989), weak forbidden oxygen lines (flux ratio [O III] λ5007/Hβ < 3), and often strong iron emission lines (high Fe II/Hβ, Osterbrock & Pogge 1985). These properties distinguish them from the population of Seyfert 1 galaxies (broad-line Seyfert 1s, BLS1s). Indeed, NLS1s are part of the so-called population A of the AGN main sequence (Sulentic et al. 2002; Sulentic & Marziani 2015; Marziani et al. 2018). In the soft X-ray, NLS1s also have extreme properties, that is, steep spectra (Brandt et al. 1997; Leighly 1999, $\Gamma_{\rm NLS1} = 2.19 \pm 0.10$ vs. $\Gamma_{\rm BLS1} = 1.78 \pm 0.11$) and fast and large-amplitude variability (Boller et al. 1996), with some showing X-ray flares up to a factor of 100 in flux, on time-scales of days, while BLS1s are generally seen to vary by a factor of a few. These distinctive properties (e.g., Peterson et al. 2004) are customarily understood in terms of low-mass (10^6–10^8 $M_\odot$) central black holes and higher accretion rates, close to the Eddington limit (but see, Viswanath et al. 2019). Hence, these are sources that are

possibly in an early stage of evolution (Mathur 2000). A small fraction of NLS1s (4–7%, Komossa et al. 2006; Cracco et al. 2016) have been found to be radio-loud[1] ($S_{\rm radio}/S_{\rm optical} > 10$) and show a flat radio spectrum (Oshlack et al. 2001; Zhou et al. 2003; Yuan et al. 2008; see also, Lähteenmäki et al. 2017). Additionally, some show a hard spectral component and hard X-ray spectral variability (Foschini et al. 2009).

The further, smaller subclass of γ-ray emitting NLS1 (γ-NLS1) galaxies was recently added to the picture, as a consequence of their detection at high energies ($E > 100$ MeV) by *Fermi*-LAT (PMN J0948+0022, Abdo et al. 2009a,b; Foschini et al. 2010). The γ-NLS1 now include about 35 objects (e.g. Romano et al. 2018; Foschini et al. 2021, 2022) whose properties strongly resemble those of jetted sources (see, e.g. Foschini 2012; Foschini et al. 2015; D'Ammando et al. 2016). The calculated jet power ($10^{42.6}$–$10^{45.6}$ erg s^{-1}, Foschini et al. 2015), for instance, is lower than that of flat spectrum radio quasars (FSRQs) and partially overlaps that of BL Lacertae objects (BL Lac). Furthermore, the spectral energy distributions (SEDs) of γ-NLS1 galaxies resemble the typical double-humped one of those of other jetted sources such as FSRQs and BL Lacs, as reported in Abdo et al. (2009a,b) and more recently in Foschini et al. (2010, 2015). In particular, Fig. 1 in Foschini et al. (2010) shows the SED of PMN J0948+0022 as compared to the average SEDs of FSRQs and BL Lacs as well as of those of representative radio galaxies such as NGC 6251, M 87, and Centaurus A. The SED of the prototypical γ-NLS1 PMN J0948+0022 lies between those of high-power FSRQs and low-power BL Lacs, which is not surprising given the value of the jet power reported above. Since the radio luminosity function of γ-NLS1 is a continuation (at low luminosity) of that of FSRQs, it is possible that γ-NLS1 are FSRQs in an early stage of their life cycle (Berton et al. 2016, 2017) and the possible differences in observed host galaxies could be explained by ongoing or recent mergers (e.g., Järvelä et al. 2018; Paliya et al. 2020; Shao et al. 2023, but see Varglund et al. 2022 where only one jetted NLS1 shows signs of interaction).

SDSS J164100.10+345452.7 (Zhou et al. 2006), hereon J1641, is a nearby NLS1 ($z = 0.16409 \pm 0.00002$, Albareti et al. 2017) hosted in a spiral galaxy (Olguín-Iglesias et al. 2020), initially classified as radio-quiet. Lähteenmäki et al. (2018), who observed this source 71 times at 37 GHz with the 13.7 m radio telescope at Aalto University Metsähovi Radio Observatory, reported, however, a double detection of J1641 (detection percentage of 2.8%), with an average flux of $S_{\rm 37\,GHz,ave} = 0.37$ Jy, and a maximum flux of 0.46 Jy. Since such detections typically suggest the presence of jets, they also sought J1641 in the *Fermi*-LAT data and obtained a value of $S_{\rm E>100\,MeV} = (12.5 \pm 2.18) \times 10^{-9}$ ph cm^{-2} s^{-1} (with a maximum-likelihood test statistics TS = 39), making this a radio-emitting γ-NLS1. This detection, combined with the Metsähovi detection of six more radio-silent NLS1s and one more radio-quiet NLS1, puts a severe strain on the belief that so-called radio-quiet or radio-silent NLS1s hosted in spiral galaxies are unable to launch jets. New radio observations at low frequencies suggest that the emission of the jet in these objects is absorbed, possibly via a free-free mechanism (Berton et al. 2020; Järvelä et al. 2021). Therefore, NLS1s may harbour a previously unknown class of relativistic jets that are completely undetectable at low radio frequencies, which is where most observations have been carried out to date. J1641 is now part of the sample of approximately one hundred NLS1s frequently monitored at 37 GHz at Metsähovi (Lähteenmäki et al. 2017).

In this paper, we report on a two-year multi-wavelength (optical, ultra-violet, and X-ray) monitoring of J1641 with the *Neil Gehrels Swift* Observatory (Gehrels et al. 2004) that was performed in 2019–2021 simultaneously with 37 GHz observations obtained as part of the Metsähovi NLS1 monitoring program. In particular, we focus on a 37 GHz flare observed on 2020-05-24 to 2020-05-26. In Sect. 2, we describe the observations and the data reduction. In Sect. 3, we describe our analysis and present our results, while in Sect. 4, we discuss their implications. We adopt the usual Λ-cold dark matter (Λ-CDM) cosmology (Komatsu et al. 2011) with $H_0 = 70$ km s^{-1} Mpc^{-1}, $\Omega_{\rm m} = 0.27$, and $\Omega_\Lambda = 0.73$ to facilitate direct comparison with the results in Foschini et al. (2015).

2. Observations and data reduction

2.1. Swift

The *Swift* data were collected through two yearly monitoring campaigns (Target ID 11395, PI: P. Romano) with a pace of one ~ 2–3 ks observation per week from 2019-12-09 to 2020-08-17 (97 ks) and from 2021-01-31 to 2021-07-28 (68 ks) with the X–ray Telescope (XRT, Burrows et al. 2005) and the UV/Optical Telescope (UVOT, Roming et al. 2005, with the "U+B+V+all U" filter setup), for a total exposure of 165 ks (68 observations). The pace is ideal for variability studies, since the collected data make up a regular and casual sampling of the light curve of the source at a resolution over about one week, irrespective of the source flux state. We note that each observation may consist of between one and three snapshots (satellite orbits) that are just a few hours apart.

Additionally, three target of opportunity (ToO) observation campaigns (ObsIDs: 00011395030, −032, −033; 00011395035, −036; 00011395038, −039, −042, −044, −046, and −048) were obtained (PI: P. Romano) in response to a radio detection from Metsähovi on 2020-05-24 (MJD 58993–58995; see Sect. 2.2 below) for a total of 16 ks (11 observations). We note that the observing pace of these ToOs is much denser than that of the monitoring campaigns, so when timing analysis was performed, we distinguished the case of the campaign-only dataset from the full dataset. No ToO observations were obtained after the second set of radio detections recorded in 2021. Tables A.1 and A.2 report the log of the *Swift*/XRT observations for the first and second year, respectively, and include the observing sequence (ObsID), date (MJD of the middle of the observation), start and end times (UTC) of each observation, and XRT exposure time.

The *Swift*/XRT data were reduced and analysed by using standard procedures within FTOOLS[2] (v6.29b) and the calibration database CALDB[3] (v20211105). In particular, the XRT data were processed and filtered with the task XRTPIPELINE (v0.13.6). The XRT light curve was generated in the 0.3–10 keV energy range with one point per observation and one per snapshot. We used SOSTA within XIMAGE and adopted the background measured in an annular region with an inner radius of 80 pixels and an external radius of 120 pixels centred at the source position. The PSF losses and vignetting were corrected for by using the

[1] We remark that the radio loudness parameter as defined above is becoming more and more inaccurate and unreliable in properly describing these sources, as recently summarised by Berton & Järvelä (2021).

[2] https://heasarc.gsfc.nasa.gov/ftools/ftools_menu.html

[3] https://heasarc.gsfc.nasa.gov/docs/heasarc/caldb/caldb_intro.html

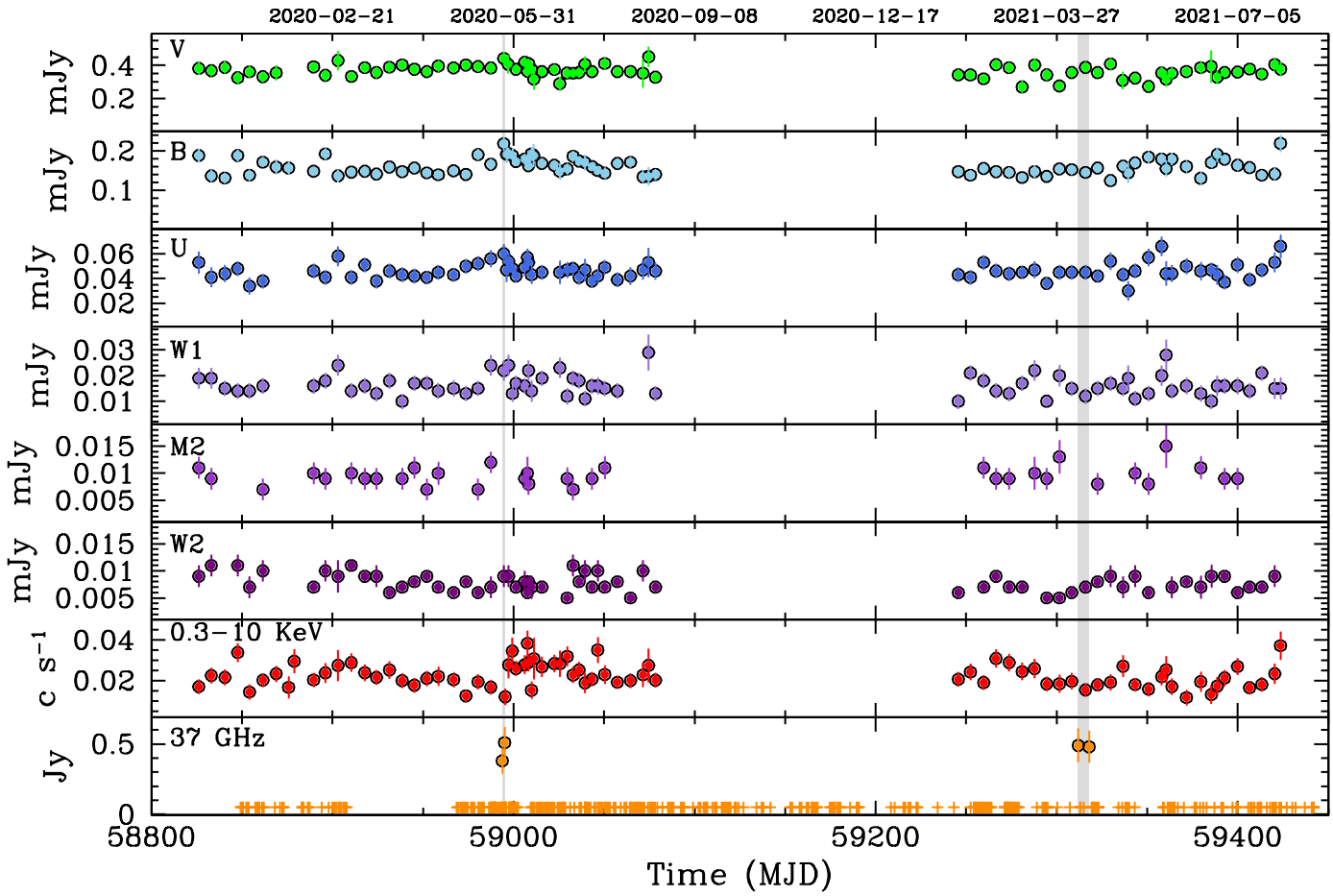

Fig. 1. Multi-wavelength light curves of SDSS J164100.10+345452.7. The optical, UV, and X-ray light curves were collected by *Swift* from 2019-12-09 to 2020-08-17 (first year campaign), from 2021-01-31 to 2021-07-28 (second year), which are shown with 1σ errorbars. The data at 37 GHz were collected at Metsähovi (<4σ non-detections represented by crosses). Grey bands mark the Metsähovi detections. Top axis reports representative dates during the campaigns.

appropriate exposure maps. In case of a non-detection, a 3σ upper limit was calculated by using SOSTA and UPLIMIT within XIMAGE and the background defined above. The XRT 0.3–10 keV light curve, binned at one bin per observation, (corresponding to one point per week during the monitoring campaign and several points per week during the ToOs) is shown in Fig. 1. We note that close to the 2020 radio flare J1641 was observed on 2020-05-25 (MJD 58994, observation 029 for 1.7 ks) and on 2020-05-27 (MJD 58996, observation 030 for ~350 s). Although these observations did not yield a detection on an individual basis (~1.1×10^{-2} counts s^{-1} at the 2.8σ level, and ~0.01 counts s^{-1} at the 1.4σ level, respectively), their combination did, at $(1.2 \pm 0.4) \times 10^{-2}$ counts s^{-1}, so we used this combination as opposed to two upper limits. On the contrary, we discarded observation 069 due to its low exposure (~350 s) and no close observations to combine it with. For the spectroscopic analysis of the XRT data, source events were extracted from a circular region with a 20 pixel radius; ancillary response files were generated with the task XRTMKARF to account for different extraction regions, vignetting, and PSF corrections; the spectral redistribution matrices in CALDB were used.

The analysis of the UVOT data, which were collected in all filters (optical *v*, *b*, *u*, and UV *w*1, *m*2, *w*2), was performed with the tasks UVOTMAGHIST, UVOTIMSUM, and UVOTSOURCE included in FTOOLS (v6.31 and CALDB v20211108, which offer a check for frames affected by small scale sensitivity, SSS, issues[4]). UVOTMAGHIST was used to identify the frames of each UVOT image affected by SSS issues and to generate a light curve in each filter at the frame level (the best time resolution available), UVOTIMSUM to sum the sky images for UVOTSOURCE to calculate the magnitude of the source through aperture photometry within a circular region centred on the best source position. This was done by applying the required corrections related to the specific detector characteristics. We adopted circular regions with radii of 5″ and 18″ for the source and background, respectively. We also discarded the source detections that yielded magnitudes with an error > 0.3 mag. The observed light curves (in units of mJy) binned at one point per observation are shown in the six top panels of Fig. 1.

2.2. Metsähovi

The Aalto University Metsähovi Radio Observatory in Finland operates a 13.7 m radio telescope, used for monitoring of AGN at 22 and 37 GHz. The NLS1 monitoring program, fully described in Lähteenmäki et al. (2017), started in 2012 and is currently ongoing. The measurements are carried out with a 1 GHz band dual-beam receiver centred at 36.8 GHz, with typical integration times between 1200 and 1800 s. The detection limit is

[4] https://swift.gsfc.nasa.gov/analysis/uvot_digest/sss_check.html

Table 1. Fractional variability in different energy bands.

	ObsID		Snapshot	
Filter	$F_{\rm var}^{\rm camp}$	$F_{\rm var}^{\rm full}$	$F_{\rm var}^{\rm camp}$	$F_{\rm var}^{\rm full}$
V	–	–	–	–
B	0.09 ± 0.01	0.09 ± 0.01	0.10 ± 0.02	0.11 ± 0.01
U	0.04 ± 0.06	–	0.02 ± 0.11	–
$W1$	0.13 ± 0.04	0.13 ± 0.04	–	–
$M2$	–	–	–	–
$W2$	0.07 ± 0.05	0.07 ± 0.05	0.11 ± 0.06	0.10 ± 0.06
X-ray	0.16 ± 0.03	0.16 ± 0.03	0.11 ± 0.04	0.13 ± 0.04

Notes. The X-ray band is 0.3–10 keV. The values are calculated for light curves drawn from campaign-only observations ($F_{\rm var}^{\rm camp}$) and the full set of observations ($F_{\rm var}^{\rm full}$), binned both at the observation level and at the snapshot level. Missing values are cases where variability is not well detected.

Table 2. Doubling and halving times.

	ObsID		Snapshot	
D/R	R	D	R	D
$\tau_{\rm d}$	1.25	1.70	0.053	5.90
$\sigma(\tau_{\rm d})$	3.9	3.2	5.0	4.7
$CR(t_1)$	0.015 ± 0.004	0.029 ± 0.004	0.012 ± 0.003	0.017 ± 0.006
$CR(t_2)$	0.031 ± 0.010	0.015 ± 0.004	0.027 ± 0.006	0.045 ± 0.013
t_1	59009.9084	59008.3476	59259.6634	59371.5824
t_2	59011.1743	59009.9084	59259.7270	59379.6139

Notes. The minimum doubling time (rise, R) and halving time (decay, D) $\tau_{\rm d}$ are in units of days and their significance is $\sigma(\tau_{\rm d})$. t_1 and t_2 are the times (MJD) when we measure the count rates, $CR(t_1)$ and $CR(t_2)$ (count s^{-1}). The values are calculated for light curves drawn from the data binned both at the observation level and at the snapshot level.

on the order of 0.2 Jy under optimal conditions. Data points with a signal-to-noise ratio (S/N) of <4 are handled as non-detections. They may occur either because the source is too faint or because of compromised weather conditions. In the latter case the measurement is discarded. Fainter sources, such as NLS1s, commonly flicker around the detection limit, frequently causing non-detections among the possibly rare detections that occur only when the peak of a flare is seen. The main flux calibrator is DR21, with NGC 7027, 3C 274, and 3C 84 used as secondary calibrators. The full data reduction procedure is reported in Teräsranta et al. (1998).

J1641 is normally observed at least once a week and during more intensive periods, for example, multi-frequency campaigns or flares, even daily. It has now been detected several times since the early reports in Lähteenmäki et al. (2018), with a maximum flux density of 0.65±0.12 Jy on 2019-09-07. In Fig. 1 (bottom panel), we show the data that are simultaneous with the *Swift* campaigns. Four detections were achieved, on 2020-05-24 (MJD 58993.7820, flux density of 0.38±0.09 Jy), 2020-05-26 (MJD 58995.0987, 0.51±0.11 Jy), 2021-04-07 (MD 59311.9087, 0.49±0.12 Jy), and 2021-04-13 (MJD 59317.8955, 0.48±0.11 Jy). We hereon refer to the May 2020 detections as the 2020 flare, and the April 2021 ones as the 2021 flare. Further detections were obtained after the end of the *Swift* campaigns on 2021-08-31 (MJD 59457.7556, 0.44±0.09 Jy) and 2021-09-09 (59466.7323, 0.48± 0.09 Jy).

3. Data analysis and results

3.1. Optical, UV, and X-ray variability

As shown in Fig. 1, the *Swift* light curves show a degree of variability. To quantify it, we computed the fractional variability according to Eqs. (10) and (B2) in Vaughan et al. (2003):

$$F_{\rm var} = \sqrt{\frac{S^2 - \bar{\sigma^2}}{\bar{x}^2}} \pm \sqrt{\left(\sqrt{\frac{1}{2N}}\frac{\bar{\sigma}^2_{\rm err}}{\bar{x}^2 F_{\rm var}}\right)^2 + \left(\sqrt{\frac{\bar{\sigma}^2_{\rm err}}{N}}\frac{1}{\bar{x}}\right)^2}. \quad (1)$$

Since the ToO data (after MJD 58996) may introduce a bias towards the high and flaring states, we performed the calculation both over the full dataset ($F_{\rm var}^{\rm full}$, ToOs included) and by restricting to the campaign data only ($F_{\rm var}^{\rm camp}$). Table 1 shows the results for both, and, since they are consistent within the errors, from now on, we consider the entire dataset for our analysis. We calculated $F_{\rm var}$ from the light curves binned both at the observation and the snapshot levels. Missing values are due to cases where variability was not adequately detected (see Appendix B in Vaughan et al. 2003). We note that the fractional variability measured in J1641 is lower than the typical values reported in D'Ammando (2020) for six well-known γ-ray NLS1s. This is unsurprising, since we focused on a long-term campaign, thus reducing the impact of high flux levels as a consequence of observations triggered by flares observed in other energy bands.

The minimum variability time scale in the X-ray energy band is $t_{\rm var} = \ln(2) \times \tau_{\rm d}$ days, where $\tau_{\rm d}$ is the doubling/halving time defined by:

$$F(t_2) = F(t_1) \times 2^{(t_2 - t_1)/\tau_{\rm d}}, \quad (2)$$

and $F(t_1)$ and $F(t_2)$ are the count rates at the times, t_1 and t_2, respectively. Given that the significance of $\tau_{\rm d}$ is $\sigma(\tau_{\rm d}) = |F(t_1) - F(t_2)|/\sigma(F(t_1))$, we selected doubling/halving times with $\sigma(\tau_{\rm d}) \geq 3$. Table 2 shows the minimum doubling and halving times and their significance when the light curves are binned both at the observation and the snapshot levels. We also note that no difference was found when considering the full dataset or the campaign dataset only. Assuming $t_{\rm var} = \ln(2) \times (\min\{\tau_{\rm d}({\rm R}); \tau_{\rm d}({\rm D})\})$, we find that the minimum variability timescale is $t_{\rm var}^{\rm obs} = 0.87$ days and $t_{\rm var}^{\rm snap} = 0.04$ d or $\simeq$1 h when the light curves are binned at the observation level and at the snapshot level, respectively. In the comoving frame, $t' = t\,(1+z)$, we obtained $t'^{\rm obs}_{\rm var} = 0.75$ days and $t'^{\rm snap}_{\rm var} = 0.034$ d, respectively.

The 0.3–10 keV light curve shown in Fig. 1 is characterised by a dynamic range (maximum count rate over minimum count rate) of 3.3. To assess whether this time variability corresponds to detectable spectral variability throughout our monitoring, we calculated the hardness ratio (HR) based on the 0.3–2 keV and 2–10 keV energy bands in the same time binning as the full light curve. We then used it to check for spectral variability on timescales of about one week (the pace of the campaign). We first fit the HR with a constant and obtained (2–10 keV)/(0.3–2 keV) = 0.48 ± 0.02 ($\chi^2 = 83.4$, degrees of freedom d.o.f. = 71, null-hypothesis probability nhp= 0.149). We then performed a linear fit that is clearly consistent with the constant fit, since the first-order coefficient is consistent with 0 ($\chi^2 = 82.9$, d.o.f. = 70, nhp = 0.138). The F-test probability with respect to the constant is indeed 0.547 (0.6σ). The same procedure was applied to the whole set of observations available on J1641, thus including two archival observations performed on 2019-05-25 and 2019-08-29, along with nine observations we obtained in March 2022 as ToOs. We obtained an F-test probability with respect to the constant of 0.660 (0.95σ), so we can conclude that we did not

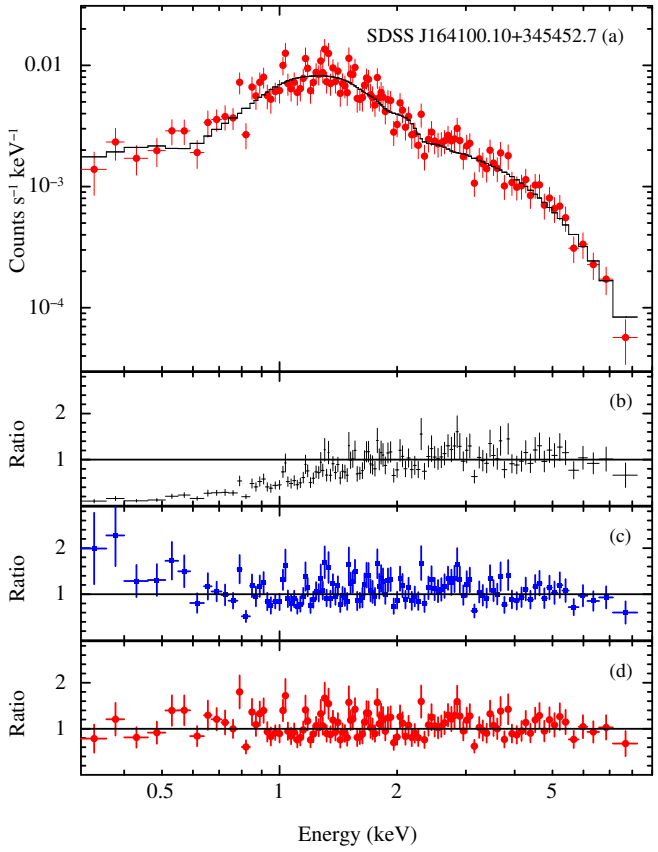

Fig. 2. *Swift*/XRT average spectrum of SDSS J164100.10+345452.7. The data are drawn from the whole two-year observing campaign (details on the spectral fits can be found in Table 3). Panel a: best fit obtained by adopting the model TBABS * ZPCFABS * ZPOWERLW; panel b: data/model ratio from the fit with TBABS * ZPOWERLW in the 2–10 keV band; panel c: data/model ratio from the fit with TBABS * ZTBABS * ZPOWERLW (0.3–10 keV); and panel d: data/model ratio from the fit with TBABS * ZPCFABS * ZPOWERLW (0.3–10 keV).

detect significant spectral variability on timescales of about one week. We note that the same conclusions are reached when the light curve is binned at the snapshot level (few snapshots within a day, separated by about a week) with F-test probabilities below 0.5σ.

3.2. X-ray time-selected spectroscopy

Given the lack of variations in the HR, we first considered two spectra, the one accumulated throughout the whole two-year campaign ('total', MJD range 58826–59423, ~181 ks exposure), and the 'flare' spectrum, close to the May 2020 radio flare (MJD 58994–58997, ~3.5 ks).

We fit the total spectrum with XSPEC (v. 12.12.0, Arnaud 1996) with a simple power-law model (ZPOWERLW, fixed redshift $z = 0.16409$) corrected for an equivalent hydrogen column corresponding to the Galactic value (fixed $N_{\rm H}^{\rm Gal} = 1.4 \times 10^{20}$ cm^{-2}, HI4PI Collaboration 2016) with the TBABS (Wilms et al. 2000) model. A fit with a neutral absorber in the whole XRT band (0.3–10 keV), yielding a hard photon index $\Gamma = 1.13 \pm 0.04$, was clearly unacceptable (nhp $\sim 10^{-26}$) due to the large negative residuals at energies below 2 keV, suggesting that further absorption was required. This is confirmed by the fact that a fit in the 2–10 keV range yielded reasonable results and a much softer photon index, $\Gamma_{2-10\,\rm keV} = 1.84 \pm 0.15$ (see Fig. 2b).

Table 3. Time-selected *Swift*/XRT spectroscopy.

Spectrum parameter	Total value	Flare value	Units
	`tbabs * zpowerlw` (2–10 keV)		
Γ_{2-10}	1.84 ± 0.15	0.94 ± 1.35	
F_{2-10}	6.24	14.1	$\times 10^{-13}$ erg cm^{-2} s^{-1}
χ^2/d.o.f.	42.40/48	12.72/20 (70.48)	
nhp	0.701	0.808	
	`tbabs * zpowerlw` (0.3–10 keV)		
$\Gamma_{0.3-10}$	1.13 ± 0.04	$0.67^{+0.38}_{-0.39}$	
$F_{0.3-10}$	10.3	17.3	$\times 10^{-13}$ erg cm^{-2} s^{-1}
χ^2/d.o.f.	359.00/118	32.98/37 (98.40)	
nhp	3.77×10^{-26}	0.658	
	`tbabs * ztbabs * zpowerlw` (0.3–10 keV)		
$N_{{\rm H},z}$	$3.2^{+0.6}_{-0.5}$	$2.6^{+5.3}_{-2.6p}$	$\times 10^{21}$ cm^{-2}
$\Gamma_{0.3-10}$	$1.75^{+0.10}_{-0.09}$	$1.08^{+0.71}_{-0.64}$	
$F_{0.3-10}$	8.71	14.5	$\times 10^{-13}$ erg cm^{-2} s^{-1}
χ^2/d.o.f.	142.83/117	33.96/36 (98.17)	
nhp	0.0525	0.566	
	`tbabs * zpcfabs * zpowerlw` (0.3–10 keV)		
$N_{{\rm H},z}$	6.2 ± 1.3	–	$\times 10^{21}$ cm^{-2}
f	$0.91^{+0.02}_{-0.03}$	–	
$\Gamma_{0.3-10}$	1.93 ± 0.12	–	
$F_{0.3-10}$	8.54	–	$\times 10^{-13}$ erg cm^{-2} s^{-1}
χ^2/d.o.f.	124.47/116	–	
nhp	0.279	–	
	`tbabs * absori * zpowerlw` (0.3–10 keV)		
$N_{{\rm H},z}$	$5.4^{+1.2}_{-1.1}$	–	$\times 10^{21}$ cm^{-2}
$\Gamma_{0.3-10}$	$1.89^{+0.12}_{-0.11}$	–	
ξ	$2.4^{+2.5}_{-2.0}$	–	$\times 10^{-2}$
$F_{0.3-10}$	8.52	–	$\times 10^{-13}$ erg cm^{-2} s^{-1}
χ^2/d.o.f.	128.51/116	–	
nhp	0.201	–	
	`tbabs * zxipcf * zpowerlw` (0.3–10 keV)		
$N_{{\rm H},z}$	$6.2^{+1.3}_{-1.8}$	–	$\times 10^{21}$ cm^{-2}
$\log \xi$	$-0.63^{+0.17}_{-1.07}$	–	
f	$0.99^{+0.01p}_{-0.04}$	–	
$\Gamma_{0.3-10}$	$2.00 \pm +0.17$	–	
$F_{0.3-10}$	8.46	–	$\times 10^{-13}$ erg cm^{-2} s^{-1}
χ^2/d.o.f.	127.88/115	–	
nhp	0.194	–	

Notes. The fits are for $z = 0.16409$ and a fixed $N_{\rm H}^{\rm Gal} = 1.4 \times 10^{20}$ cm^{-2} (TBABS). Fluxes are corrected for the Galactic absorption. For the flare spectrum, Cash statistics was used and the goodness of fit (g.o.f.) was calculated with 10^4 simulations. Uncertainties are given at 90% c.l. for one interesting parameter.

The details of the fits are reported in Table 3. To model the excess absorption we added a second absorption component local to the source (ZTBABS) obtaining $N_{{\rm H},z} = (3.2^{+0.6}_{-0.5}) \times 10^{21}$ cm^{-2} and $\Gamma = 1.75^{+0.10}_{-0.09}$ (Fig. 2c). The trend in the residuals shown in Fig. 2c, indicates that the model adopted for the extra neutral absorber may not be the most appropriate, so we considered a redshifted absorption edge (ZEDGE). The resulting fit, however, did not reach convergence, with an unphysical edge energy and an unconstrained optical depth, leading to even more prominent residuals below 1 keV. Next, we considered a neutral absorber partially covering the central source, described by a ZPCFABS component, with the redshift of this absorber fixed at the same value as that of the source. This model yielded significant improvement ($\Delta\chi^2 = -18$) over the ZTBABS and, as shown in Fig. 2d, no large-scale structure is left in the data/model ratio. The absorber is characterised by $N_{{\rm H},z} = (6.2 \pm 1.3) \times 10^{21}$ cm^{-2}, a covering fraction $f = 0.91^{+0.02}_{-0.03}$, while the underlying continuum has a photon index $\Gamma = 1.93 \pm 0.12$.

Finally, we considered the possibility that the absorber is ionised. When using an ABSORI (Done et al. 1992; Magdziarz & Zdziarski 1995; Zdziarski et al. 1995) component, with fixed absorber temperature and Iron abundance, we obtain a significant improvement ($\Delta\chi^2 = -14$) over the ZTBABS model, but a worse fit than the ZPCFABS one. The presence of an ionised absorber partially covering the central source modelled by ZXIPCF is also not supported by the data, since the fit offers no improvement over the ZPCFABS model (see Table 3).

We fit the flare spectrum, consisting of 42 photons, in the 0.3–10 keV band, with the same models as those considered for the total spectrum (see Table 3) by adopting Cash (Cash 1979) statistics. The spectrum can be satisfactorily fit even without an added absorption component. Indeed, for the TBABS * ZTBABS * ZPOWERLW, the TBABS * ZPCFABS * ZPOWERLW and TBABS * ZXIPCF * ZPOWERLW models the $N_{\mathrm{H},z}$ is consistent with zero; for the TBABS * ABSORI * ZPOWERLW model, the fit did not converge, with an ionisation parameter consistent with 0. We note, in particular, that if we fit the flare spectrum with the TBABS * ZTBABS * ZPOWERLW model with the photon index fixed to the mean value (1.75), we obtain $N_{\mathrm{H},z} = (6.1^{+4.9}_{-3.0}) \times 10^{21}\,\mathrm{cm}^{-2}$. This implies that we cannot exclude that extra absorption is indeed present.

We conclude that the total spectrum of J1641 can be best described in the X-ray by an absorbed power-law model modified by a partially covering neutral absorber (TBABS * ZPCFABS * ZPOWERLW), with a covering fraction of $f = 0.91^{+0.02}_{-0.03}$ and underlying continuum with a photon index of $\Gamma_{\mathrm{total}} = 1.93 \pm 0.12$. Conversely, the flare spectrum can be satisfactorily fit even without an added absorption component by adopting a power-law model with a very hard photon index of $\Gamma_{\mathrm{flare}} = 0.67^{+0.38}_{-0.39}$ modified just by the Galactic absorption.

Since the XRT data are spread over a 20-month baseline, and guided by the examination of the XRT light curve, we also extracted spectra in several time intervals, as detailed in Table A.3: '1st yr': all observations collected during the first year of the campaign (MJD range 58826–59078, on-source exposure of ∼113.3 ks); '2nd yr': all observations collected during the second year of the campaign (MJD range 59245–59423, ∼67.8 ks); 'pre0': all observations preceding the radio flare of 2020-05-24 (MJD range 58826–58987, ∼61 ks); 'pre1': close observations preceding the radio flare of 2020-05-24 (MJD 58938–58987, ∼22 ks); 'plateau': during an enhanced state of X-ray emission following the radio flare (MJD 59001–59029, ∼23 ks); 'post': the remainder of the first year campaign (MJD 59032–59078, ∼24 ks). Since no ToO observations were obtained after the April 2021 radio flare, recorded on 2021-04-07 and 2021-04-13, no XRT data are close enough ($\lesssim$3 d) to be considered simultaneous; therefore, we did not perform any detailed spectroscopy. We fit all spectra with the same models as those adopted for the total spectrum described above and the results are reported in full in Table A.4. In the case of the TBABS * ZPCFABS * ZPOWERLW model, we note that we obtained consistent covering factors in each time selected spectrum, therefore, we also performed a fit with the covering factor fixed to the value derived from the total spectrum, $f = 0.91$. In all cases, a simple absorbed power-law model is not an adequate description and an extra absorption component is required.

4. Discussion

We report on the first multi-wavelength *Swift* monitoring campaign performed on SDSS J164100.10+345452.7, a nearby (z = 0.16409) NLS1 formerly known as radio-quiet which was however recently detected not only in the radio, but also in the γ-rays (Lähteenmäki et al. 2018); this behaviour hints at the presence of a relativistic jet. Our *Swift* campaign, with a regular pace of one ∼2–3 ks observation per week, lasted two years and was performed with the primary goal of assessing the baseline variability properties (far from radio flares) of J1641 and to obtain matching, multi-wavelength data that are strictly simultaneous with the 37 GHz monitoring data being collected at Metsähovi (Lähteenmäki et al. 2017). Indeed, the campaign covered two distinct radio flaring episodes, one each year and for the first flare (2020-05-24 to 2020-05-26), we also obtained further ToO observations in order to have a denser sampling of the *Swift* light curves.

4.1. Spectral variability and excess absorption

From our time-selected X-ray spectroscopy (see Table A.4), we find that the source is remarkably stable during the two years of monitoring, with the notable exception of the flare spectrum, extracted almost simultaneously with the radio flare in 2020. The mean spectrum, as represented by the total one in Table 3, is best described by an absorbed power-law model (ZPOWERLW, fixed redshift $z = 0.16409$), where in addition to the Galactic absorption (TBABS, with fixed $N_{\mathrm{H}}^{\mathrm{Gal}} = 1.4 \times 10^{20}\,\mathrm{cm}^{-2}$), an additional absorber is required. We modelled this component with a partially covering ($f = 0.91^{+0.02}_{-0.03}$) neutral absorber, (ZPCFABS, see Sect. 3.2). The underlying continuum has a photon index $\Gamma_{\mathrm{total}} = 1.93 \pm 0.12$, which places J1641 in the bulk of the radio-loud γ-NLS1 population shown in Fig. 2 by Foschini et al. (2015), whose median is $\Gamma = 1.8$. Our conclusions stand when considering any of the time selections we performed, particularly those before and after the radio flare.

On the contrary, the X-ray spectrum extracted around the radio flare does not require any absorption in excess of the Galactic one and is much harder, with $\Gamma_{\mathrm{flare}} \sim 0.7 \pm 0.4$. We cannot exclude extra absorption when fitting the flare spectrum with the TBABS * ZTBABS * ZPOWERLW model with the photon index fixed to the mean value (1.75). Indeed, we obtained $N_{\mathrm{H},z} < 11 \times 10^{21}\,\mathrm{cm}^{-2}$, namely, a value that is considerably higher than that of the mean spectrum. Contrary to the averaged spectrum, in the flare case, the fit shows a hard gamma also when restricted to the hard band, thus suggesting that the source is intrinsically harder. Although it is not unphysical to interpret the simultaneous increase of the X-ray flux and absorption during the flare, we consider it more likely that we are seeing, instead, the presence of a harder spectral component distinct from the softer emission observed out of flare. We can naturally interpret these findings in terms of the jet emission emerging from a gap in the absorber. Consequently, this implies that thanks to the observed correlated radio–X-ray variability, the radio emission during the flare is indeed linked to the presence of a jet in J1641, as opposed to out-of-flare radio emission which may be dominated by star formation activity (Berton et al. 2020), as also testified by the WISE colours $W1 - W2 = 1$ and $W2 - W3 = 4.3$ (as derived from NED) which place J1641 outside of the AGN wedge (Mateos et al. 2012, 2013, see also Fig. 3 of Foschini et al. 2015 for a comparison of other radio loud NLS1 and radio loud γ-NLS1s).

We note that we also considered the possibility that the absorber is ionised, in line with the hypothesis put forth by Berton et al. (2020) that the radio emission from the relativistic jet in J1641 can be absorbed in the JVLA bands through free-free absorption due a screen of ionised gas associated with starburst activity (or shocks). And, indeed, an ABSORI component fits the

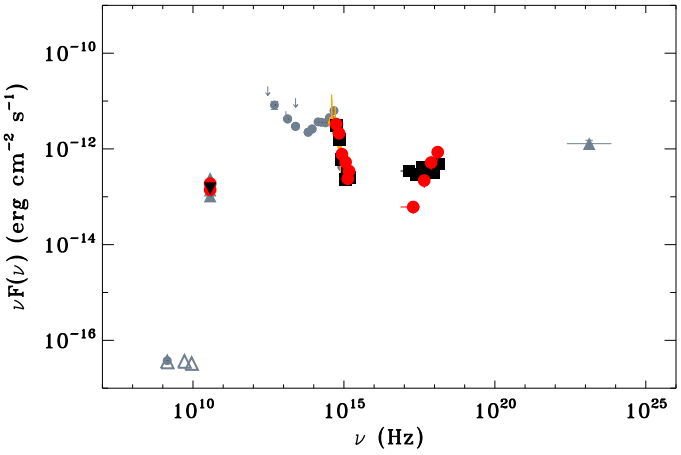

Fig. 3. Spectral energy distribution of SDSS J164100.10+345452.7. The black filled square points represent the *Swift* data obtained during the two-year *Swift* campaigns; the black filled triangle is a representative Metsähovi upper limit (0.40 Jy) calculated as an average over 15 d, while the red filled circles are the strictly simultaneous ones obtained during the flare of May 2020 (*Swift* and Metsähovi). The SDSS spectrum is shown in orange. The grey points are drawn from the literature: JVLA 1.6, 5.2, and 9 GHz data (empty triangles), Metsähovi 37 GHz data (filled triangles), and *Fermi* (filled triangles), as well as FIRST, IRAS, WISE, USNO, 2MASS, SDSS, and WGA catalogues points collected from the ASI/SSDC SED Builder Tool.

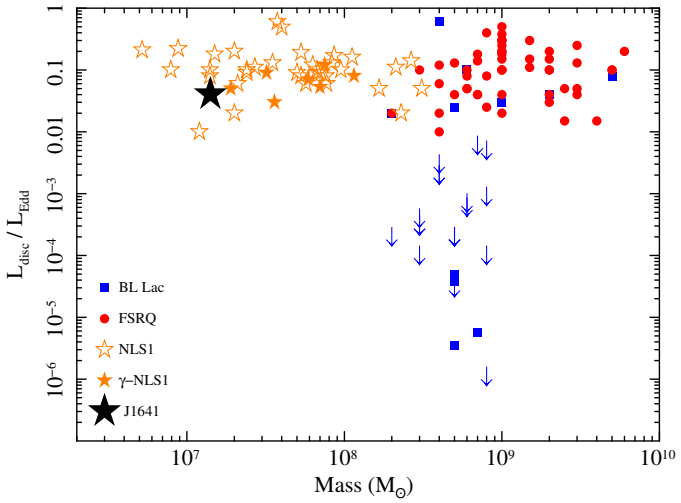

Fig. 4. Accretion disc luminosity normalised to the Eddington luminosity as a function of the black-hole mass in solar masses. The black star indicates SDSS J164100.10+345452.7. Symbols and colors are the same as those in Fig. 4 in Foschini et al. (2015).

X-ray data reasonably well, although it is not statistically as well as the neutral absorber model. More dedicated optical and X-ray spectral analysis will be presented in a companion paper (Lähteenmäki et al., in prep.) that should help shed light on the nature of the absorber.

4.2. Spectral energy distributions

In Fig. 3, we show the radio to γ-ray spectral energy distribution (SED) of J1641, which includes the data obtained during the two-year *Swift* campaigns, covering the optical/UV + X-ray energy ranges and a representative upper limit from Metsähovi (0.40 Jy), calculated as an average over 15 d, as well as the data obtained during the May 2020 flare (*Swift* and Metsähovi). We note that this flaring SED is the first strictly simultaneous broad-band SED (radio + optical/UV + X-ray) obtained for this source. The archival SDSS spectrum[5] is shown in orange. The grey points, instead, represent historical data drawn from the literature, and they include: JVLA (1.6, 5.2, and 9 GHz, empty triangles, Berton et al. 2020), Metsähovi (37 GHz, filled triangles, Lähteenmäki et al. 2018), and *Fermi* (filled triangles, Lähteenmäki et al. 2018). We also report data from FIRST, IRAS, WISE, USNO, 2MASS, SDSS, and WGA catalogues, as collected from the ASI/SSDC SED Builder Tool[6] (Stratta et al. 2011), which include public catalogues and surveys.

The SED of J1641 resembles those of other jetted sources, with a hint of a double-humped shape. However, we do not have a strictly simultaneous *Fermi*/LAT detection during the radio flare, therefore it is difficult to constrain the whole SED. We note, however, that the SED of J1641 resemble those of other γ-ray NLS1 galaxies, with a synchrotron peak below $\nu_{\rm syn}^{\rm peak} \approx 10^{13}$ Hz, a host galaxy component peaking at a few $\times 10^{14}$ Hz (as a comparison with a Sb galaxy template indicates), and the X-ray data that could be modelled with a synchrotron self-Compton component (see e.g., Abdo et al. 2009c; Foschini et al. 2015). While the optical-UV data during the May 2020 flare (red points) seem consistent with the average two-year *Swift* campaigns (black points), the 0.3–10 keV data during the flare have a notably harder spectrum than the average one.

[5] https://skyserver.sdss.org/dr17/
[6] https://tools.ssdc.asi.it/SED

4.3. Energetics

In the following, we compute the quantities related to the physical processes occurring in J1641 and compare them with those of other γ-ray NLS1s. Following the procedure in Berton et al. (2021), we first estimated the luminosity of the Hβ emission line, $L_{\rm H\beta} = 2.51 \times 10^{41}$ erg s^{-1}, and used it to calculate the distance of the broad-line region (BLR) from Greene et al. (2010, Table 2),

$$\log\left[\frac{R_{\rm BLR}}{10\,\text{light day}}\right] = 0.85 + 0.53\log\left[\frac{L_{\rm H\beta}}{10^{43}\,\text{erg s}^{-1}}\right], \quad (3)$$

which implies $R_{\rm BLR} \simeq 2.6 \times 10^{16}$ cm. The BLR luminosity is calculated according to,

$$L_{\rm BLR} = 21.2 \times L_{\rm H\beta}\,(\text{erg s}^{-1}) \simeq 5.3 \times 10^{42}\,\text{erg s}^{-1}. \quad (4)$$

The BLR radiation energy density is then derived from the BLR radius and luminosity,

$$u_{\rm BLR} = \frac{L_{\rm BLR}}{4\,\pi\,R_{\rm BLR}^2\,c}(\text{erg cm}^{-3}) \simeq 0.02\,\text{erg cm}^{-3}. \quad (5)$$

Given $R_{\rm BLR}$, we can estimate the accretion disc luminosity (see e.g., Ghisellini & Tavecchio 2009):

$$L_{\rm disc} = 10^{45} \times \left(\frac{R_{\rm BLR}}{10^{17}\,\text{cm}}\right)^2 (\text{erg s}^{-1}) \simeq 6.8 \times 10^{43}\,\text{erg s}^{-1}, \quad (6)$$

which can be normalised to the Eddington luminosity,

$$L_{\rm Edd} = 1.26 \times 10^{38}\left(\frac{M_{\rm BH}}{M_\odot}\right)(\text{erg s}^{-1}) \simeq 1.8 \times 10^{45}\,\text{erg s}^{-1}, \quad (7)$$

Table 4. Overall properties of SDSS J164100.10+345452.7.

Parameter	Value	Units
$M_{\rm BH}$ [(a)]	1.41	$\times 10^7\,M_\odot$
$L_{\rm H\beta}$	2.51	$\times 10^{41}$ erg s^{-1}
$L_{\rm Edd}$	1.8	$\times 10^{45}$ erg s^{-1}
$L_{\rm disc}$	6.8	$\times 10^{43}$ erg s^{-1}
$L_{\rm disc}/L_{\rm Edd}$	0.04	–
$R_{\rm BLR}$	2.6	$\times 10^{16}$ cm
$L_{\rm BLR}$	5.3	$\times 10^{42}$ erg s^{-1}
$u_{\rm BLR}$	0.02	erg cm^{-3}
$\alpha_{1.6-5.2\,\rm GHz}$	1.04	–
$\alpha_{5.2-9.0\,\rm GHz}$	1.24	–
$\alpha_{9.0-37\,\rm GHz}$	−4.92	–
$S_{15\,\rm GHz}$	4.33	mJy
$L_{15\,\rm GHz}$	1.95	$\times 10^{40}$ erg s^{-1}
$P_{\rm jet}^{\rm rad}$	1.65	$\times 10^{42}$ erg s^{-1}
$P_{\rm jet}^{\rm kin}$	1.83	$\times 10^{42}$ erg s^{-1}
$P_{\rm jet}^{\rm tot}$	3.48	$\times 10^{42}$ erg s^{-1}

Notes. [(a)]From Järvelä et al. (2015).

assuming $M_{\rm BH} = 1.41 \times 10^7\,M_\odot$ as computed in Järvelä et al. (2015). We obtain $L_{\rm disc}/L_{\rm Edd} \simeq 0.04$.

Figure 4 shows the position of J1641 (black filled star) in the $L_{\rm disc}/L_{\rm Edd}$–$M_{\rm BH/M_\odot}$ plane. Open (filled) orange stars mark the place of NLS1 (γ-ray-NLS1) objects, respectively. This plot is adapted from Fig. 4 in Foschini et al. (2015) where red circles are FSRQs and the blue squares are BL Lac objects (blue arrows indicate upper limits in the accretion luminosity). We note that J1641 fits in the region of the γ-ray NLS1 galaxies well.

Another important quantity that characterises jetted sources is the jet power. Foschini (2014) established two relations between the radiative and kinetic jet power and the luminosity at 15 GHz:

$$\log(P_{\rm jet}^{\rm rad}) = (12 \pm 2) + (0.75 \pm 0.04)\ \log(L_{\rm radio}^{\rm core})\,{\rm erg\,s^{-1}}, \quad (8)$$

$$\log(P_{\rm jet}^{\rm kin}) = (6 \pm 2) + (0.90 \pm 0.04)\ \log(L_{\rm radio}^{\rm core})\,{\rm erg\,s^{-1}}. \quad (9)$$

Järvelä et al. (2021) have provided simultaneous radio fluxes at 1.6, 5.2, 9.0 GHz from the *Karl G. Jansky* Very Large Array (JVLA) and 37 GHz data from the Metsähovi Radio Observatory (non-simultaneous with the JVLA). From these data, we can estimate the radio spectral index[7] $\alpha_{9.0-37\,\rm GHz} \simeq -4.9$, obtaining $S_{15\,\rm GHz} = 4.3$ mJy, when assuming:

$$\alpha_{1,2} = -\frac{\log(S_1/S_2)}{\log(\nu_1/\nu_2)}, \quad (10)$$

with $S_{9.0\,\rm GHz} = 0.35$ mJy and $S_{37\,\rm GHz} = 370.0$ mJy. The K-corrected luminosity equation,

$$L = 4\pi D_{\rm lum}^2\,\nu S_\nu\,(1+z)^{(\alpha_{9.0-37\,\rm GHz}-1)}, \quad (11)$$

yields $L_{15\,\rm GHz} = 1.95 \times 10^{40}$ erg s^{-1} and allows us to estimate $P_{\rm jet}^{\rm rad} = 1.65 \times 10^{42}$ erg s^{-1}, $P_{\rm jet}^{\rm kin} = 1.83 \times 10^{42}$ erg s^{-1}, and $P_{\rm jet}^{\rm tot} = 3.48 \times 10^{42}$ erg s^{-1}. We note that $\log(P_{\rm jet}^{\rm tot}) \simeq 42.54$ erg s^{-1} is similar to the lowest value in Table 3 of Foschini et al. (2015), corresponding to J0706+3901, whose physical values (see Table 2 in Foschini et al. 2015) are similar to those of J1641. In Table 4, we summarise the results of our calculations.

[7] This value needs to be considered with caution as the data are not simultaneous.

5. Summary and conclusions

In this paper we present a 20-month *Swift* monitoring campaign performed, for the first time, on the newly recognised (Lähteenmäki et al. 2018) γ-NLS1 galaxy SDSS J164100.10+345452.7, which is regularly being observed at the Metsähovi Radio Observatory at the 37 GHz frequency. Our investigation has indeed led us to the following findings and conclusions.

- We observe minor, but significant variability in the light curves, with an $F_{\rm var}$, as calculated in the UVOT and XRT energy bands, smaller than the values reported in the literature for the best six well-known γ-NLS1s, whose light curves, however, are biased towards flaring states.
- During the *Swift* campaign, two radio flares were observed at Metsähovi and, for the first one (May 2020), it was possible to obtain further *Swift* observations that closely matched the radio ones.
- From the analysis of the X-ray spectra both preceding and following the radio flare, we find that a simple absorbed power-law model is not adequate and extra absorption is required. Indeed, the average spectrum of J1641 can be best described by an absorbed power-law model with a photon index $\Gamma = 1.93 \pm 0.12$, modified by a partially covering neutral absorber (covering fraction $f = 0.91^{+0.02}_{-0.03}$).
- The X-ray spectrum closest to the radio flare, however, does not require extra absorption and is much harder ($\Gamma_{\rm flare} \sim 0.7 \pm 0.4$). This implies the emergence of an additional, harder spectral component that we interpret as the jet emission peeking out of a gap in the absorber.
- For this flaring state, we present (also for the first time) a strictly simultaneous SED covering the radio, optical/UV, and X-ray energy bands afforded by the combination of *Swift* and Metsähovi data. A comparison with the average SED (see Fig. 3) for this object, highlights the harder X-ray spectrum during the radio flare. No obvious variations are observed in the optical, however.
- Overall, the SED, although it is not well constrained at high energies due to the lack of simultaneous *Fermi*/LAT data, does show a resemblance to the SEDs of jetted sources, with hints at the presence of two humps. The SED of J1641 is reminiscent of other γ-NLS1 galaxies with a synchrotron peak below 10^{13} Hz, a host galaxy component peaking at a few 10^{14} Hz, and the X-ray data which could be modelled with a synchrotron self-Compton component (Abdo et al. 2009c; Foschini et al. 2015).
- Assuming that the radio emission is due to a jet, we can then calculate its power, $\log(P_{\rm jet}^{\rm tot}) \simeq 42.54$ erg s^{-1}, which is one of the lowest measured when compared with the Foschini et al. (2015) sample, and reminiscent of the γ-NLS1 J0706+3901.

In conclusion, our observations show how a dedicated and well-paced monitoring campaign covering simultaneously the radio (at high frequencies) and the X-ray energy bands can allow us to interpret the source properties observed in different emission states. In particular, in the case of SDSS J164100.10+345452.7, we have been able to detect the 'smoking-gun' of the so-called 'absorbed jet', originally proposed by Berton et al. (2020). Indeed, the simultaneity and co-spatiality of the radio and X-ray emission show that the nucleus is responsible for the observed flaring of the source. Furthermore, if the origin of the flare were a putative extended emission, detected by JVLA but unresolved by Metsähovi, we would also observe a kpc-scale source with a variability timescale of days, which is not physically possibile. Currently, our knowledge of the

absorbed jets is still limited, and only new observations in the X-rays will allow us to confirm if they all show signs of absorption.

Acknowledgements. We thank the anonymous referee for comments that helped to improve the paper. We acknowledge unwavering support from Amos. This work has been partially supported by the ASI-INAF program I/004/11/4. We acknowledge financial contribution from the agreement ASI-INAF n. 2017-14-H.0. This publication makes use of data obtained at Metsähovi Radio Observatory, operated by Aalto University in Finland. We acknowledge the use of public data from the *Swift* data archive. This research has made use of the NASA/IPAC Extragalactic Database (NED) which is operated by the Jet Propulsion Laboratory, California Institute of Technology, under contract with the National Aeronautics and Space Administration. Part of this work is based on archival data, software or online services provided by the Space Science Data Center – ASI. Happy 18th, *Swift*.

References

Abdo, A. A., Ackermann, M., Ajello, M., et al. 2009a, ApJ, 699, 976
Abdo, A. A., Ackermann, M., Ajello, M., et al. 2009b, ApJ, 707, 727
Abdo, A. A., Ackermann, M., Ajello, M., et al. 2009c, ApJ, 707, L142
Albareti, F. D., Allende Prieto, C., Almeida, A., et al. 2017, ApJS, 233, 25
Arnaud, K. A. 1996, ASP Conf. Ser., 101, 17
Berton, M., & Järvelä, E. 2021, Astron. Nachr., 342, 1066
Berton, M., Caccianiga, A., Foschini, L., et al. 2016, A&A, 591, A98
Berton, M., Foschini, L., Caccianiga, A., et al. 2017, Front. Astron. Space Sci., 4, 8
Berton, M., Järvelä, E., Crepaldi, L., et al. 2020, A&A, 636, A64
Berton, M., Peluso, G., Marziani, P., et al. 2021, A&A, 654, A125
Boller, T., Brandt, W. N., & Fink, H. 1996, A&A, 305, 53
Brandt, W. N., Mathur, S., & Elvis, M. 1997, MNRAS, 285, L25
Burrows, D. N., Hill, J. E., Nousek, J. A., et al. 2005, Space Sci. Rev., 120, 165
Cash, W. 1979, ApJ, 228, 939
Cracco, V., Ciroi, S., Berton, M., et al. 2016, MNRAS, 462, 1256
D'Ammando, F. 2020, MNRAS, 496, 2213
D'Ammando, F., Orienti, M., Finke, J., et al. 2016, Galaxies, 4, 11
Done, C., Mulchaey, J. S., Mushotzky, R. F., & Arnaud, K. A. 1992, ApJ, 395, 275
Foschini, L. 2012, Proceedings of Nuclei of Seyfert Galaxies and QSOs - Central Engine and Conditions of Star Formation (Seyfert 2012). 6–8 November
Foschini, L. 2014, Int. J. Mod. Phys. Conf. Ser., 28, 1460188P
Foschini, L., Maraschi, L., Tavecchio, F., et al. 2009, Adv. Space Res., 43, 889
Foschini, L., Fermi/Lat Collaboration, Ghisellini, G., et al. 2010, ASP Conf. Ser., 427, 243
Foschini, L., Berton, M., Caccianiga, A., et al. 2015, A&A, 575, A13
Foschini, L., Lister, M. L., Antón, S., et al. 2021, Universe, 7, 372
Foschini, L., Lister, M. L., Andernach, H., et al. 2022, Universe, 8, 587
Gehrels, N., Chincarini, G., Giommi, P., et al. 2004, ApJ, 611, 1005
Ghisellini, G., & Tavecchio, F. 2009, MNRAS, 397, 985
Goodrich, R. W. 1989, ApJ, 342, 224
Greene, J. E., Hood, C. E., Barth, A. J., et al. 2010, ApJ, 723, 409
HI4PI Collaboration (Ben Bekhti, N., et al.) 2016, A&A, 594, A116
Järvelä, E., Lähteenmäki, A., & León-Tavares, J. 2015, A&A, 573, A76
Järvelä, E., Lähteenmäki, A., & Berton, M. 2018, A&A, 619, A69
Järvelä, E., Berton, M., & Crepaldi, L. 2021, Front. Astron. Space Sci., 8, 147
Komatsu, E., Smith, K. M., Dunkley, J., et al. 2011, ApJS, 192, 18
Komossa, S., Voges, W., Xu, D., et al. 2006, AJ, 132, 531
Lähteenmäki, A., Järvelä, E., Hovatta, T., et al. 2017, A&A, 603, A100
Lähteenmäki, A., Järvelä, E., Ramakrishnan, V., et al. 2018, A&A, 614, L1
Leighly, K. M. 1999, ApJS, 125, 317
Magdziarz, P., & Zdziarski, A. A. 1995, MNRAS, 273, 837
Marziani, P., Dultzin, D., Sulentic, J. W., et al. 2018, Front. Astron. Space Sci., 5, 6
Mateos, S., Alonso-Herrero, A., Carrera, F. J., et al. 2012, MNRAS, 426, 3271
Mateos, S., Alonso-Herrero, A., Carrera, F. J., et al. 2013, MNRAS, 434, 941
Mathur, S. 2000, MNRAS, 314, L17
Olguín-Iglesias, A., Kotilainen, J., & Chavushyan, V. 2020, MNRAS, 492, 1450
Oshlack, A. Y. K. N., Webster, R. L., & Whiting, M. T. 2001, ApJ, 558, 578
Osterbrock, D. E., & Pogge, R. W. 1985, ApJ, 297, 166
Paliya, V. S., Pérez, E., García-Benito, R., et al. 2020, ApJ, 892, 133
Peterson, B. M., Ferrarese, L., Gilbert, K. M., et al. 2004, ApJ, 613, 682
Romano, P., Vercellone, S., Foschini, L., et al. 2018, MNRAS, 481, 5046
Roming, P. W. A., Kennedy, T. E., Mason, K. O., et al. 2005, Space Sci. Rev., 120, 95
Shao, X., Gu, M., Chen, Y., et al. 2023, ApJ, 943, 136
Stratta, G., Capalbi, M., Giommi, P., et al. 2011, ArXiv e-prints [arXiv:1103.0749]
Sulentic, J., & Marziani, P. 2015, Front. Astron. Space Sci., 2, 6
Sulentic, J. W., Marziani, P., Zamanov, R., et al. 2002, ApJ, 566, L71
Teräsranta, H., Tornikoski, M., Mujunen, A., et al. 1998, A&AS, 132, 305
Varglund, I., Järvelä, E., Lähteenmäki, A., et al. 2022, A&A, 668, A91
Vaughan, S., Edelson, R., Warwick, R. S., & Uttley, P. 2003, MNRAS, 345, 1271
Viswanath, G., Stalin, C. S., Rakshit, S., et al. 2019, ApJ, 881, L24
Wilms, J., Allen, A., & McCray, R. 2000, ApJ, 542, 914
Yuan, W., Zhou, H. Y., Komossa, S., et al. 2008, ApJ, 685, 801
Zdziarski, A. A., Johnson, W. N., Done, C., Smith, D., & McNaron-Brown, K. 1995, ApJ, 438, L63
Zhou, H.-Y., Wang, T.-G., Dong, X.-B., Zhou, Y.-Y., & Li, C. 2003, ApJ, 584, 147
Zhou, H., Wang, T., Yuan, W., et al. 2006, ApJS, 166, 128

Appendix A: Supplementary tables and figures

Table A.1. *Swift*/XRT observation log of SDSS J164100.10+345452.7.

Sequence	Date MJD (mid)	Start time (UT) (yyyy-mm-dd hh:mm:ss)	End time (UT) (yyyy-mm-dd hh:mm:ss)	Exposure (s)
00011395003	58826.13783	2019-12-09 01:31:03	2019-12-09 05:05:53	2502
00011395004	58833.07074	2019-12-16 00:39:51	2019-12-16 02:43:52	2959
00011395005	58840.58190	2019-12-23 13:04:59	2019-12-23 14:50:53	2688
00011395006	58847.64448	2019-12-30 09:09:11	2019-12-30 21:46:54	2913
00011395007	58854.17679	2020-01-06 00:07:15	2020-01-06 08:21:53	2166
00011395008	58861.57894	2020-01-13 12:09:26	2020-01-13 15:37:54	3009
00011395009	58868.89399	2020-01-20 19:39:46	2020-01-20 23:14:54	2620
00011395010	58875.75798	2020-01-27 17:18:31	2020-01-27 19:04:26	1198
00011395011	58878.85233	2020-01-30 20:13:49	2020-01-30 20:40:52	1622
00011395013	58889.60558	2020-02-10 08:05:12	2020-02-10 20:58:52	3249
00011395014	58896.07517	2020-02-17 00:51:35	2020-02-17 02:44:53	2332
00011395015	58903.10809	2020-02-24 01:45:18	2020-02-24 03:25:59	1036
00011395017	58910.44720	2020-03-02 02:37:02	2020-03-02 18:50:54	2740
00011395018	58917.85224	2020-03-09 17:54:33	2020-03-09 22:59:53	2766
00011395019	58924.30035	2020-03-16 03:14:06	2020-03-16 11:10:53	3084
00011395020	58931.50555	2020-03-23 10:21:05	2020-03-23 13:54:53	2465
00011395021	58938.50374	2020-03-30 11:08:53	2020-03-30 13:01:52	2670
00011395022	58945.20770	2020-04-06 04:02:16	2020-04-06 05:55:54	2735
00011395023	58952.08435	2020-04-13 00:23:01	2020-04-13 03:39:54	2786
00011395024	58958.45545	2020-04-19 09:04:47	2020-04-19 12:46:53	2833
00011395025	58966.92002	2020-04-27 21:03:45	2020-04-27 23:05:53	3162
00011395026	58973.76286	2020-05-04 17:17:08	2020-05-04 19:19:52	2771
00011395027	58980.43370	2020-05-11 08:40:08	2020-05-11 12:08:55	2630
00011395028	58987.48241	2020-05-18 00:14:28	2020-05-18 22:54:52	2397
00011395029	58994.64205	2020-05-25 15:10:11	2020-05-25 15:38:54	1723
00011395030[a]	58996.16110	2020-05-27 03:49:06	2020-05-27 03:54:52	346
00011395032[a]	58997.30146	2020-05-28 00:31:22	2020-05-28 13:56:53	1484
00011395033[a]	58999.38572	2020-05-30 02:03:05	2020-05-30 16:27:46	1504
00011395034	59001.38639	2020-06-01 01:50:55	2020-06-01 16:41:52	3365
00011395035[a]	59006.16589	2020-06-05 19:03:53	2020-06-06 12:53:52	2344
00011395036[a]	59007.69577	2020-06-07 09:21:56	2020-06-08 00:01:53	2079
00011395037	59008.34756	2020-06-08 07:22:05	2020-06-08 09:18:52	2949
00011395038[a]	59009.90842	2020-06-09 20:15:22	2020-06-09 23:20:53	2129
00011395039[a]	59011.17429	2020-06-11 04:06:03	2020-06-11 04:15:52	589
00011395040	59015.69333	2020-06-15 11:38:54	2020-06-15 21:37:53	2608
00011395041	59022.49924	2020-06-22 09:21:53	2020-06-22 14:35:54	2705
00011395042[a]	59025.58544	2020-06-25 09:12:09	2020-06-25 18:53:53	1229
00011395043	59029.60794	2020-06-29 11:59:58	2020-06-29 17:10:53	2630
00011395044[a]	59032.92782	2020-07-02 21:16:13	2020-07-02 23:15:53	2655
00011395045	59036.21290	2020-07-06 00:15:16	2020-07-06 09:57:52	2680
00011395046[a]	59039.52393	2020-07-09 09:26:49	2020-07-09 15:42:06	1319
00011395047	59043.34032	2020-07-13 07:10:15	2020-07-13 09:09:52	3016
00011395048[a]	59046.52746	2020-07-16 05:16:12	2020-07-16 20:02:53	1647
00011395049	59050.35234	2020-07-20 06:37:52	2020-07-20 10:16:52	2344
00011395050	59057.34706	2020-07-27 07:19:39	2020-07-27 09:19:53	3056
00011395051	59064.65346	2020-08-03 11:24:03	2020-08-03 19:57:54	2873
00011395052	59071.58888	2020-08-10 12:27:25	2020-08-10 15:48:33	1176
00011395053	59074.64927	2020-08-13 15:29:00	2020-08-13 15:40:52	712
00011395054	59078.43118	2020-08-17 03:45:55	2020-08-17 16:55:52	2766

Notes. For the first year of monitoring, we report the observing sequence, date (MJD of the middle of the observation), start and end times (UTC), and XRT exposure time. [a] Data obtained through additional ToOs in response to the Metsähovi detection on 2020-05-24.

Table A.2. *Swift*/XRT observation log of SDSS J164100.10+345452.7.

Sequence	Date MJD	Start time (UT) (yyyy-mm-dd hh:mm:ss)	End time (UT) (yyyy-mm-dd hh:mm:ss)	Exposure (s)
00011395055	59245.65652	2021-01-31 14:00:52	2021-01-31 17:29:53	2698
00011395056	59252.36437	2021-02-07 02:13:29	2021-02-07 15:15:52	2848
00011395057	59259.69355	2021-02-14 15:41:32	2021-02-14 17:35:52	2743
00011395058	59266.49648	2021-02-21 00:36:59	2021-02-21 23:12:53	2776
00011395059	59273.73557	2021-02-28 15:49:32	2021-02-28 19:28:53	2778
00011395060	59280.93881	2021-03-07 21:33:52	2021-03-07 23:29:54	2846
00011395061	59287.71487	2021-03-14 14:32:54	2021-03-14 19:45:54	2209
00011395062	59294.52133	2021-03-21 09:20:25	2021-03-21 15:40:52	2944
00011395063	59301.51512	2021-03-28 11:26:00	2021-03-28 13:18:52	1745
00011395064	59308.35169	2021-04-04 07:29:58	2021-04-04 09:22:53	2630
00011395065	59315.91731	2021-04-11 21:04:58	2021-04-11 22:56:52	2658
00011395066	59322.55583	2021-04-18 12:21:55	2021-04-18 14:18:51	2994
00011395067	59329.76132	2021-04-25 16:32:42	2021-04-25 19:59:53	2357
00011395068	59336.60402	2021-05-02 09:31:43	2021-05-02 19:27:51	1705
00011395069	59339.52500	2021-05-05 12:33:08	2021-05-05 12:38:51	344
00011395070	59343.31562	2021-05-09 01:05:06	2021-05-09 14:03:52	2964
00011395071	59350.73554	2021-05-16 15:54:28	2021-05-16 19:23:52	2389
00011395072	59357.94372	2021-05-23 21:47:01	2021-05-23 23:30:53	2101
00011395073	59360.49007	2021-05-26 11:37:31	2021-05-26 11:53:51	980
00011395074	59363.58868	2021-05-29 00:29:31	2021-05-30 03:45:52	1971
00011395075	59371.64900	2021-06-06 13:47:13	2021-06-06 17:21:53	2209
00011395076	59379.58760	2021-06-14 13:14:24	2021-06-14 14:57:53	2131
00011395077	59385.45068	2021-06-20 07:30:58	2021-06-20 14:06:59	1522
00011395078	59388.67917	2021-06-23 15:25:06	2021-06-23 17:10:53	1439
00011395079	59392.72476	2021-06-27 16:29:23	2021-06-27 18:17:54	2733
00011395080	59399.82883	2021-07-04 17:12:08	2021-07-04 22:34:53	2866
00011395081	59406.49739	2021-07-11 10:11:35	2021-07-11 13:40:52	2788
00011395082	59413.33648	2021-07-18 06:15:08	2021-07-18 09:53:54	2455
00011395083	59420.43584	2021-07-25 10:14:19	2021-07-25 10:40:54	1595
00011395084	59423.62380	2021-07-28 14:46:40	2021-07-28 15:09:52	1392

Notes. For the second year of monitoring, we report the observing sequence, date (MJD of the middle of the observation), start and end times (UTC), and XRT exposure time.

Table A.3. Time-selected *Swift*/XRT spectroscopy: Time ranges.

Spectr. Name	ObsID range	Start time (UT)	End time (UT)	Expo. (ks)
total	003–084	2019-12-09 01:31:04	2021-07-28 15:09:52	181.07
1st year	003–054	2019-12-09 01:31:04	2020-08-17 16:55:53	113.3
2nd year	055–084	2021-01-31 14:00:52	2021-07-28 15:09:52	67.8
pre0	003–028	2019-12-09 01:31:04	2020-05-18 22:54:52	61.334
pre1	021–028	2020-03-30 11:08:54	2020-05-18 22:54:52	21.984
flare	029–032	2020-05-25 15:10:12	2020-05-28 13:56:49	3.553
plateau	034–043	2020-06-01 01:50:56	2020-06-29 17:10:54	22.626
post	044–054	2020-07-02 21:16:14	2020-08-17 16:55:53	24.246

Table A.4. Time-selected *Swift*/XRT spectroscopy: Results.

	tbabs * zpowerlw (2–10 keV)				
		Γ_{2-10}	F_{2-10}	χ^2/d.o.f.	
total		$1.84^{+0.15}_{-0.15}$	6.23	42.40/48	
1st year		$1.75^{+0.22}_{-0.21}$	6.55	28.15/31	
2nd year		$1.77^{+0.23}_{-0.23}$	5.84	36.08/17	
pre0		$1.79^{+0.34}_{-0.33}$	6.14	17.41/15	
pre1		$1.70^{+0.79}_{-0.73}$	5.88	5.02/3	
flare		$0.94^{+1.35}_{-1.35}$	14.1	12.72/20 (70.48)	
plateau		$1.93^{+0.62}_{-0.61}$	6.5	4.01/4	
post		$1.61^{+0.68}_{-0.67}$	7.15	3.49/4	
	tbabs * zpowerlw (0.3–10 keV)				
		$\Gamma_{0.3-10}$	$F_{0.3-10}$	χ^2/d.o.f.	
flare		$0.67^{+0.38}_{-0.39}$	17.2	32.98/37 (98.40)	
	tbabs * ztbabs * zpowerlw (0.3–10 keV)				
	$N_{\rm H,z}$	$\Gamma_{0.3-10}$	$F_{0.3-10}$	χ^2/d.o.f.	
total	$3.2^{+0.6}_{-0.5}$	$1.75^{+0.10}_{-0.09}$	8.64	142.83/117	
1st year	$2.8^{+0.6}_{-0.5}$	$1.72^{+0.12}_{-0.11}$	9.00	87.05/79	
2nd year	$3.8^{+1.2}_{-1.0}$	$1.78^{+0.17}_{-0.16}$	8.00	70.11/44	
pre0	$2.6^{+0.9}_{-0.7}$	$1.71^{+0.17}_{-0.16}$	8.57	40.80/41	
pre1	$2.7^{+1.9}_{-1.2}$	$1.66^{+0.31}_{-0.27}$	8.11	13.40/12	
flare	$2.6^{+5.3}_{-2.6p}$	$1.08^{+0.71}_{-0.64}$	14.4	33.96/36 (98.17)	
v plateau	$2.2^{+1.2}_{-0.9}$	$1.76^{+0.26}_{-0.24}$	9.95	20.99/17	
post	$3.2^{+2.0}_{-1.4}$	$1.65^{+0.33}_{-0.29}$	9.32	17.62/16	
	tbabs * absori * zpowerlw (0.3–10 keV)				
	$N_{\rm H,z}$	$\Gamma_{0.3-10}$	ξ	$F_{0.3-10}$	χ^2/d.o.f.
total	$5.4^{+1.2}_{-1.1}$	$1.89^{+0.12}_{-0.11}$	$2.4^{+2.5}_{-2.0}$	8.45	128.51/116
1st year	$4.3^{+1.3}_{-1.4}$	$1.83^{+0.14}_{-0.15}$	$1.1^{+2.9}_{-1.0}$	8.80	83.11/78
2nd year	$6.6^{+2.3}_{-2.1}$	$1.94^{+0.20}_{-0.19}$	$4.3^{+9.4}_{-3.0}$	7.81	62.08/43
pre0	$4.2^{+1.8}_{-2.1}$	$1.84^{+0.20}_{-0.23}$	$1.4^{+4.0}_{-1.4p}$	8.35	39.50/40
pre1	$5.8^{+5.5}_{-4.0}$	$1.89^{+0.48}_{-0.42}$	$5.0^{+5.7}_{-5.0p}$	7.73	11.98/11
plateau	$4.1^{+3.5}_{-2.5}$	$1.92^{+0.36}_{-0.32}$	$1.8^{+10.5}_{-1.8p}$	9.60	19.52/16
1 post	$6.4^{+3.9}_{-3.3}$	$1.88^{+0.39}_{-0.36}$	$6.4^{+40.8}_{-6.4}$	8.78	14.43/15
	tbabs * zpcfabs * zpowerlw (0.3–10 keV)				
	$N_{\rm H,z}$	f	$\Gamma_{0.3-10}$	$F_{0.3-10}$	χ^2/d.o.f.
total	$6.2^{+1.3}_{-1.3}$	$0.91^{+0.02}_{-0.03}$	$1.93^{+0.12}_{-0.12}$	8.45	124.47/116
1st year	$4.7^{+1.5}_{-1.5}$	$0.91^{+0.06}_{-0.05}$	$1.84^{+0.15}_{-0.15}$	8.82	82.25/78
2nd year	$7.6^{+2.5}_{-2.3}$	$0.92^{+0.03}_{-0.04}$	$2.00^{+0.21}_{-0.20}$	7.81	59.48/43
pre0	$4.1^{+2.3}_{-1.6}$	$0.92^{+0.01p}_{-0.07}$	$1.81^{+0.23}_{-0.20}$	8.42	39.41/40
pre1	$6.2^{+5.7}_{-4.2}$	$0.90^{+0.01p}_{-0.14}$	$1.90^{+0.51}_{-0.22}$	7.76	12.26/11
plateau	$5.3^{+4.2}_{-1.8}$	$0.88^{+0.01p}_{-0.12}$	$1.98^{+0.41}_{-0.36}$	9.56	19.19/16
post	$6.8^{+4.1}_{-3.5}$	$0.91^{+0.07}_{-0.11}$	$1.91^{+0.42}_{-0.38}$	8.77	14.42/15
1st year	$4.6^{+1.5}_{-1.2}$	0.91	1.84 ± 0.15	8.82	82.26/79
2nd year	$7.6^{+2.4}_{-2.2}$	0.91	$1.99^{+0.15}_{-0.18}$	7.84	59.50/44
pre0	$4.2^{+2.2}_{-1.5}$	0.91	$1.81^{+0.22}_{-0.20}$	8.42	39.42/41
pre1	$6.2^{+5.4}_{-4.1}$	0.91	$1.93^{+0.35}_{-0.48}$	7.65	12.38/12
plateau	$4.7^{+5.1}_{-2.9}$	0.91	$2.00^{+0.38}_{-0.41}$	9.41	19.69/17
post	$6.9^{+3.8}_{-3.6}$	0.91	$1.93^{+0.27}_{-0.39}$	8.69	14.45/16

Notes. The fits are for $z = 0.16409$ and a fixed $N_{\rm H}^{\rm Gal} = 1.4 \times 10^{20}$ cm^{-2} (TBABS). Absorption columns $N_{\rm H,z}$ are in units of $\times 10^{21}$ cm^{-2}, the ionisation parameter, ξ, in units of $\times 10^{-2}$, while the observed fuxes are in units of $\times 10^{-13}$ erg cm^{-2} s^{-1}. For the flare spectrum, Cash statistics was used and the goodness of fit (g.o.f.) was calculated with 10^4 simulations. Uncertainties are given at 90 % c.l. for one interesting parameter.